Nanoscale

PAPER

View Article Online
View Journal | View Issue

Cite this: *Nanoscale*, 2018, **10**, 2944

High-capacity and long-life lithium storage boosted by pseudocapacitance in three-dimensional MnO–Cu–CNT/graphene anodes†

Junyong Wang, Qinglin Deng, Mengjiao Li, Kai Jiang, Zhigao Hu * and Junhao Chu

Boosting the lifespan of MnO-based materials for future lithium ion batteries is one of the primary challenges due to the intrinsic low ionic conductivity and volume expansion during the conversion process. Herein, superior lithium storage in a new quaternary MnO–Cu–CNT/graphene composite has been demonstrated, which is boosted by pseudocapacitance benefitting from the three-dimensional CNT/graphene and nanosized Cu additives. Such architecture offers highly interpenetrated porous conductive networks in intimate contact with MnO–Cu grains and abundant stress buffer space for effective charge transport upon cycling. The ternary MnO–Cu–graphene electrode contributes an ever-increasing reversible capacity of 938.3 mA h g^{-1} after 800 cycles at 0.8 A g^{-1}. In particular, the quaternary MnO–Cu–CNT/graphene electrode demonstrates a high specific capacity of 1334 mA h g^{-1} at 0.8 A g^{-1} after 800 cycles and long lifetimes of more than 3500 cycles at 5 A g^{-1} with a capacity of 557.9 mA h g^{-1} and close-to-100% Coulombic efficiency. The boosted pseudocapacitive lithium storage together with the simple material fabrication method in a MnO–Cu–CNT/graphene hybrid could pave the way for the development of high-capacity and long-life energy storage devices.

Received 3rd November 2017,
Accepted 3rd January 2018

DOI: 10.1039/c7nr08191j

rsc.li/nanoscale

1. Introduction

Lithium ion batteries (LIBs) play an unparalleled role in the markets of consumer electronics and newly emerging large-scale applications owing to their high energy density, long lifespan and no memory effect.[1–4] Problematically, the current commercial graphite anode with a low theoretical specific capacity of 372 mA h g^{-1} and poor rate performance no longer satisfies the growing demand of stronger power and higher energy densities. Therefore, enormous investigations have been dedicated to the exploitation of high-capacity and long-cycle-life anode materials, such as Si,[5,6] metal,[7,8] transitional metal oxides,[9–12] and sulfides.[13–15] Among them, manganese oxides have attracted extensive attention due to their environmental benignity, resource abundance, low conversion potential, low voltage hysteresis (<0.7 V), and high theoretical capacity.[16–18] Particularly, MnO can deliver a high energy density of 5.43 g cm^{-3} due to its lower electrochemical motivation force value of 1.032 V *vs.* Li/Li^+, thereby highlighting itself as one of the most promising anode materials for LIBs.[19,20] Unfortunately, like other metal oxide anodes, the realization of the application of MnO-based materials as LIB anodes is hampered by the unavoidably decayed capacity upon cycling and inferior rate capability, mainly induced by the intrinsically sluggish kinetics, self-aggregation and the drastic volumetric change during the repeated charge/discharge process.[21,22]

To this end, substantial efforts have been devoted to design advantageous structures and fabricate hybrids with conductive agents to alleviate the above problems of MnO-based anode materials. One effective strategy is hybridizing or coating metal oxides with functional carbon materials such as graphene,[23–25] and carbon nanotubes (CNTs), which is favorable for ameliorating the electrical conductivity, alleviating the volume expansion and increasing the electrode/electrolyte contact area. In addition, the sagacious design of nanostructures such as three-dimensional (3D) hierarchical hybrid architecture can effectively relieve the structural strain induced by the cycling process and accelerate the diffusion of lithium ions for providing additional channels.[26,27] Moreover, incorporating transition metal nanocrystals into MnO-based materials boosts the stability of the conversion reactions and high rate capability by preventing the aggregation of active materials and improves the electron transfer kinetics for high active surface/inter-

Key Laboratory of Polar Materials and Devices (MOE) and Technical Center for Multifunctional Magneto-Optical Spectroscopy (Shanghai), Department of Electronic Engineering, East China Normal University, Shanghai 200241, China.
E-mail: zghu@ee.ecnu.edu.cn; Fax: +86-21-54345119; Tel: +86-21-54345150

†Electronic supplementary information (ESI) available. See DOI: 10.1039/C7NR08191J

face.[28,29] This novel and simple material design strategy has been realized in other metal oxides-based anode materials for high performance lithium storage.[30]

Despite these great endeavors, however, the rate performance and long-term cycling stability are still unsatisfactory for promising LIB application due to its intrinsically slow solid-state lithium diffusion. Compared with the conventional diffusion-controlled storage, pseudocapacitive storage can greatly boost the rate capability and lengthen the battery life through fast faradaic charge-transfer reactions including surface redox reactions and bulk fast ion intercalation.[31,32] So far, capacitive-like storage has been realized in various metal oxides (Nb_2O_5, V_2O_5, TiO_2, *etc.*) with enhanced electrochemical performance.[33–35] Particularly, MnO-based materials with pseudocapacitive storage have also been prepared in recent years. For example, conformal nanoscale MnO/graphene exhibits an upward trend of reversible capacity, which was mainly assigned to the extra interfacial lithium storage.[36] RGO–MnO–RGO sandwich nanostructures with enhanced pseudocapacitance have been demonstrated as advanced anodes for LIBs by combining the surface-controlled and diffusion-controlled behavior simultaneously.[37] Therefore, modifying surface pseudocapacitance to achieve high-rate capability and long-term stability lithium storage for MnO-based anode materials is of significant importance.

Herein, we demonstrate highly reversible and long-life lithium storage boosted by the pseudocapacitance behaviour originating from the novel quaternary MnO–Cu–CNT/graphene composite, which was identified by qualitative kinetic analysis. The formation of nanosized Cu and MnO grains anchored on three-dimensional CNT/graphene networks efficiently elevates the kinetics of charge transfer during conversion reactions. Such purposely engineered interconnected architecture can adapt well to the volume variation, prevent the aggregation of MnO and boost the transport rates of lithium ions into the internal parts of the electrode matrix. In particular, the enlarged accessible surface area and unique porosity contribute significantly to the pseudocapacitive storage due to the well-developed electrode–electrolyte contact and mass-transportation channels. All these merits result in encouraging electrochemical performance including highly stable reversibility and long cycle life at high current density in the MnO–Cu–CNT/graphene hybrid.

2. Experimental

2.1. Material preparation

Graphene oxide (GO) was prepared by the oxidation of natural graphite flakes following a modified Hummer's method. CNTs were obtained from XFNANO Materials Tech Co., Ltd (Nanjing, China) and treated in a mixture of concentrated H_2SO_4/HNO_3 (3 : 1) at 80 °C under constant magnetic stirring for 2 h. The as-prepared CNTs were purified by centrifuging and washing with deionized (DI) water to remove the residual acid and then the acidified CNTs were obtained upon vacuum drying at 60 °C. The CNT/graphene networks were prepared by using a homogeneous GO/CNTs suspension. Briefly, 20 mg CNTs was first added to 20 mL DI water and then intensively ultra-sonicated using an ultrasonication probe (1000 W) for 20 min to form a uniform suspension. After that, 30 mL GO aqueous dispersion (2 mg mL^{-1}) was added into the as-prepared CNT aqueous dispersion under stirring until a homogeneous mixture was obtained. The mixture was then intensively ultrasonicated to form a homogeneous CNT/graphene suspension.

The MnO–Cu–CNT/graphene (CG) composite was prepared using a one-step process. In a typical procedure, 1 mmol $Mn(Ac)_2{\cdot}4H_2O$ and $Cu(Ac)_2{\cdot}H_2O$ were dissolved in the as-prepared GO/CNT suspension under magnetic stirring for 2 h. Then, the pH of the mixed solution was adjusted by adding 4.4 g NaOH and stirred for another 2 h. The solution was sealed in a 100 mL Teflon-lined stainless steel autoclave at 180 °C for 24 h. After the autoclave cooled down to room temperature, the black products were collected and washed with DI water and absolute alcohol alternately. The final samples were vacuum-dried at 60 °C for 12 h and annealed at 600 °C in a tube furnace under a N_2 atmosphere for two hours. For comparison, MnO–Cu–graphene (G), MnO–graphene (G) and other MnO–Cu–CNT/graphene with different Cu content were prepared while keeping other conditions constant.

2.2. Materials characterization

X-ray diffraction (XRD) analyses were performed on a Bruker D8 diffractometer equipped with Cu-Kα radiation (λ = 1.5418 Å) at a scanning speed of 10° min^{-1} from 10° to 80°. The N_2 adsorption/desorption isotherms, Brunauer–Emmett–Teller (BET) surface area and DFT pore size distribution were measured by a TriStar II 3020 instrument. X-ray photoelectron spectroscopy (XPS) was conducted on a RBD upgraded PHI-5000C ESCA system (PerkinElmer) with Mg-Kα radiation ($h\nu$ = 1253.6 eV). Scanning electron microscopy (SEM) images were obtained on a PHILIPS XL30TMP system. Transmission electron microscopy (TEM) and high-resolution TEM (HRTEM) were performed on an FEI Tecnai G20 TEM at an operation voltage of 200 kV.

2.3. Electrochemical characterization

The lithium ion storage behavior of the as-prepared materials was studied in 2032 coin-type cells by using lithium foil as the counter electrode and Cellgard 2400 as the separator. Cell assembly was carried out in an Argon-filled glovebox with the concentrations of the moisture and oxygen below 1 ppm. LiPF6 (1 M) dissolved in ethylene carbonate/dimethyl carbonate/ethyl methyl carbonate (1 : 1 : 1, in vol) was used as the electrolyte. The working electrodes were prepared by pasting homogeneous slurries consisting of the as-prepared materials (70 wt%), acetylene black (20 wt%), and polyvinylidene fluoride binder (10 wt%) dissolved in *N*-methyl-2-pyrrolidone onto a pure Cu foil, followed by vacuum drying at 100 °C for 12 h. The mass loading of the active material in the electrode was ~0.8 mg cm^{-2}. The galvanostatic charge and discharge tests were conducted on a Land CT 2001A battery testing system in

the potential window between 0.02 and 3.0 V *vs.* Li/Li^+. Cyclic voltammetry (CV) tests were conducted on a CHI660D electrochemical workstation at various scan rates in the voltage range of 0.02–3.0 V *vs.* Li/Li^+. Electrochemical impedance spectroscopy (EIS) was performed by applying a sine wave with an amplitude of 5 mV over the frequency range from 100 kHz to 0.01 Hz.

3. Results and discussion

The crystal structures and morphologies of the MnO–G, MnO–Cu–G and MnO–Cu–CG composites were characterized. The XRD patterns are shown and compared in Fig. 1a. Sharp diffraction peaks at 2θ = 34.9°, 40.6°, 58.8°, 70.3° and 73.9° can be indexed to the (111), (200), (220), (311) and (222) diffraction planes of cubic phase MnO (JCPDS# 07-0230), respectively, revealing the good crystallinity of MnO in the as-prepared composites. For MnO–Cu–G and MnO–Cu–CG, two major peaks at 43.3° and 50.5° corresponding to the (111) and (200) planes were observed, indicating the existence of crystalline Cu. It is also noted that the broad hump at 23° is in accord with the characteristic peak (002) of graphite and the weak diffraction peak at about 26.5° is assigned to CNTs in the MnO–Cu–CG composite.[25] N_2 absorption–desorption isotherms were obtained to evaluate the porosity of the MnO–Cu–CG architecture structure. As shown in Fig. 1b, a type IV with hysteresis loops between the adsorption and desorption isotherm curves represents the mesoporous characteristics. The Barrett–Joyner–Halenda (BJH) method was applied to calculate the pore-size distribution. The result shows the mesopores with a size of 4.5 nm. The Brunauer–Emmett–Teller (BET) result confirms that the surface area is 59.9 $m^2\ g^{-1}$ for the MnO–Cu–CG composite, much higher than that for MnO–Cu–G (19.0 $m^2\ g^{-1}$, Fig. S1†) and MnO–Cu–CNT (16.0 $m^2\ g^{-1}$, Fig. S2†). Such mesoporous architecture with a high surface area is favorable for efficient electrolyte penetration and rapid lithium ion diffusion. Moreover, it is also able to accommodate the volume expansion of MnO during the charge/discharge process, which is highly favorable for the electrochemical performance enhancement as an electrode. X-ray photoelectron spectroscopy (XPS) analyses were performed to further examine the chemical state and composition. The characteristic peaks of C 1s, O 1s, Cu 2p and Mn 2p were observed in a wide scan spectrum in Fig. S3,† further confirming the successful synthesis of MnO–Cu–CG. Fig. 1c reveals the high resolution spectrum of C 1s, which can be resolved into three peaks centered at 284.6, 286.1 and 288.8 eV, corresponding to the sp^2-hybridized graphite carbon, C–O and C═O,[24,38] respectively. The high resolution spectrum of Mn 2p (Fig. 1d) exhibits two peaks at 642.1 eV for Mn $2p_{3/2}$ and 653.5 eV for Mn $2p_{1/2}$, a typical characteristic of the MnO phase.[26]

For better observation of the morphology and architecture of the MnO–Cu–CG, MnO–Cu–G, and MnO–Cu composites, SEM and TEM were performed. As shown in Fig. 2a and

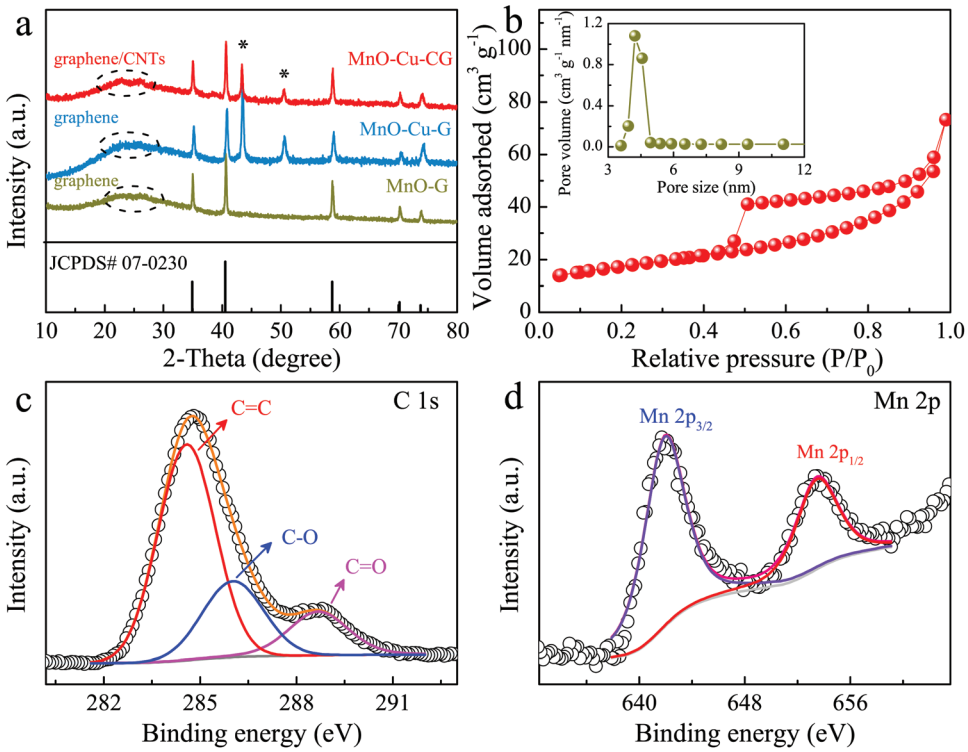

Fig. 1 (a) XRD patterns of the as-prepared MnO–Cu–CG, MnO–Cu–G and MnO–G composites; (b) N_2 adsorption–desorption isotherms of the MnO–Cu–CG composite, inset shows the pore size distribution curve; (c) high resolution XPS spectra of C 1s for the MnO–Cu–CG composite; and (d) high resolution XPS spectra of Mn 2p for the MnO–Cu–CG composite.

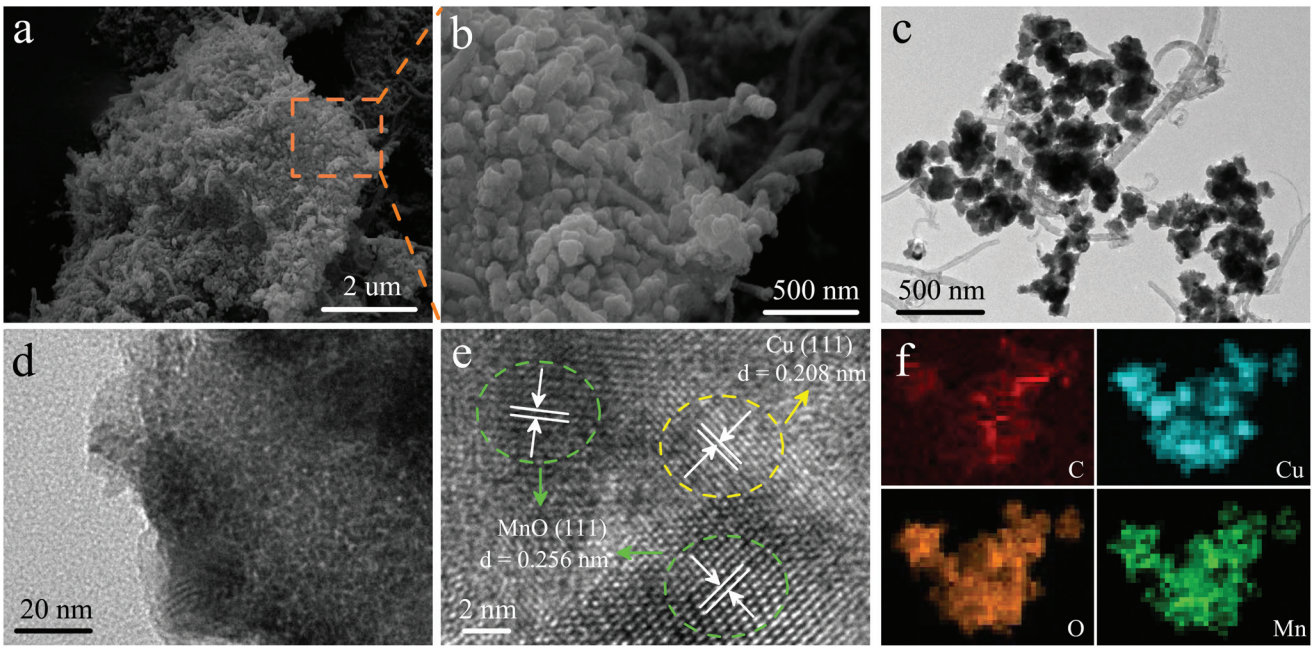

Fig. 2 (a) SEM and (b) high-magnification SEM images of the MnO–Cu–CG composite; (c) TEM and (d) high-magnification TEM images of the MnO–Cu–CG composite; (e) HRTEM image of the MnO–Cu–CG composite; and (f) element mapping of the MnO–Cu–CG composite for C, Cu, O, and Mn.

Fig. S4,† all as-prepared materials exhibit dense morphology with closely packed particles. In particular, the MnO–Cu–CG nanocomposite shows an interconnected feature with MnO–Cu aggregations well distributed in the CNT/graphene carbon nanoframeworks. The magnified SEM image of Fig. 2b, marked by a dotted orange square in Fig. 2a, further reveals that the MnO–Cu–CG composite is actually an aggregation of many small grains with a size of 50–100 nm. These ultrafine MnO nanoparticles supported on the conductive networks are favorable for the diffusion of lithium ions.[39] The TEM image in Fig. 2c further confirms that the multiscaled MnO–Cu grains are anchored to the graphene matrix and the CNTs are cross-linked with graphene sheets. The magnified TEM image in Fig. 2d reveals the well-mixed MnO and nanosized Cu in intimate contact with each other. The high resolution TEM (HRTEM) image (Fig. 2e) clearly demonstrates the existence of primarily nanocrystalline MnO and Cu. Each MnO nanoparticle exhibits single crystalline feature with fine lattice fringes of 0.252 and 0.225 nm, corresponding to the (111) and (200) plane of MnO, respectively. The lattice spacing of 0.208 nm can be indexed to the (111) plane of Cu. Specifically, the energy dispersive X-ray spectroscopy (EDS) mapping images in Fig. 2f further reveal the uniform distribution of the Mn, Cu, O and C elements in the whole network, suggesting the homogeneous distribution of the MnO and Cu nanoparticles across the CNT/graphene matrix.

For evaluating the electrochemical performance, MnO–Cu–CG, MnO–Cu–G, and MnO–G were investigated as anode materials of lithium-ion batteries. As shown in Fig. 3a–c, the three electrodes show similar CV behaviors in the first five cycles, indicating the electrochemical inertness of metallic Cu and CNT to lithium. Fig. 3a reveals that a spiculate peak at about 0.1 V along with a slope peak at 0.45 V are found in the first cathodic scan, in accordance with previous reports.[22,36] In this process, two kinds of reaction take place: (1) the reversible redox reaction of MnO to metallic Mn ($MnO + 2Li^+ + 2e^- \rightarrow Mn + Li_2O$) and (2) the irreversible reaction associated with the electrolyte decomposition and formation of the solid electrolyte interface (SEI) layer. However, this cathodic peak shifts to high voltage in the following cycles, representing the improved kinetics and an irreversible phase transformation of the microstructure. It stems from the reduction of manganese oxides and the formation of Li_2O in the hybrid electrode.[40,41] The oxidation peak centered around 1.3 V contributes to the oxidation reaction of metallic Mn to MnO ($Mn + Li_2O \rightarrow MnO + 2Li^+ + 2e^-$), which remained after further cycling.[22] Meanwhile, the weak oxidation peak at about 2.1 V corresponds to the further oxidation of Mn^{2+} to higher oxidation states due to the boosted charge-transfer kinetics and the reaction activity in the electrode, which can contribute extra reversible capacity for the MnO–Cu–CG electrode.[18,37] Moreover, the subsequent CV curves of the MnO–Cu–CG electrode are apt to overlap as compared with the MnO–Cu–G and MnO–G electrode, indicating the gradually increased cyclic durability of the electrochemical reaction for the MnO–Cu–CG electrode.

To elucidate the electrochemical kinetics of the active materials, CV curves at various sweep rates were determined. Fig. 3d–f present the representative CV curves of the MnO–Cu–CG, MnO–Cu–G, and MnO–G electrodes at various sweep rates ranging from 0.1 to 1.0 mV s^{-1}, respectively. All the redox

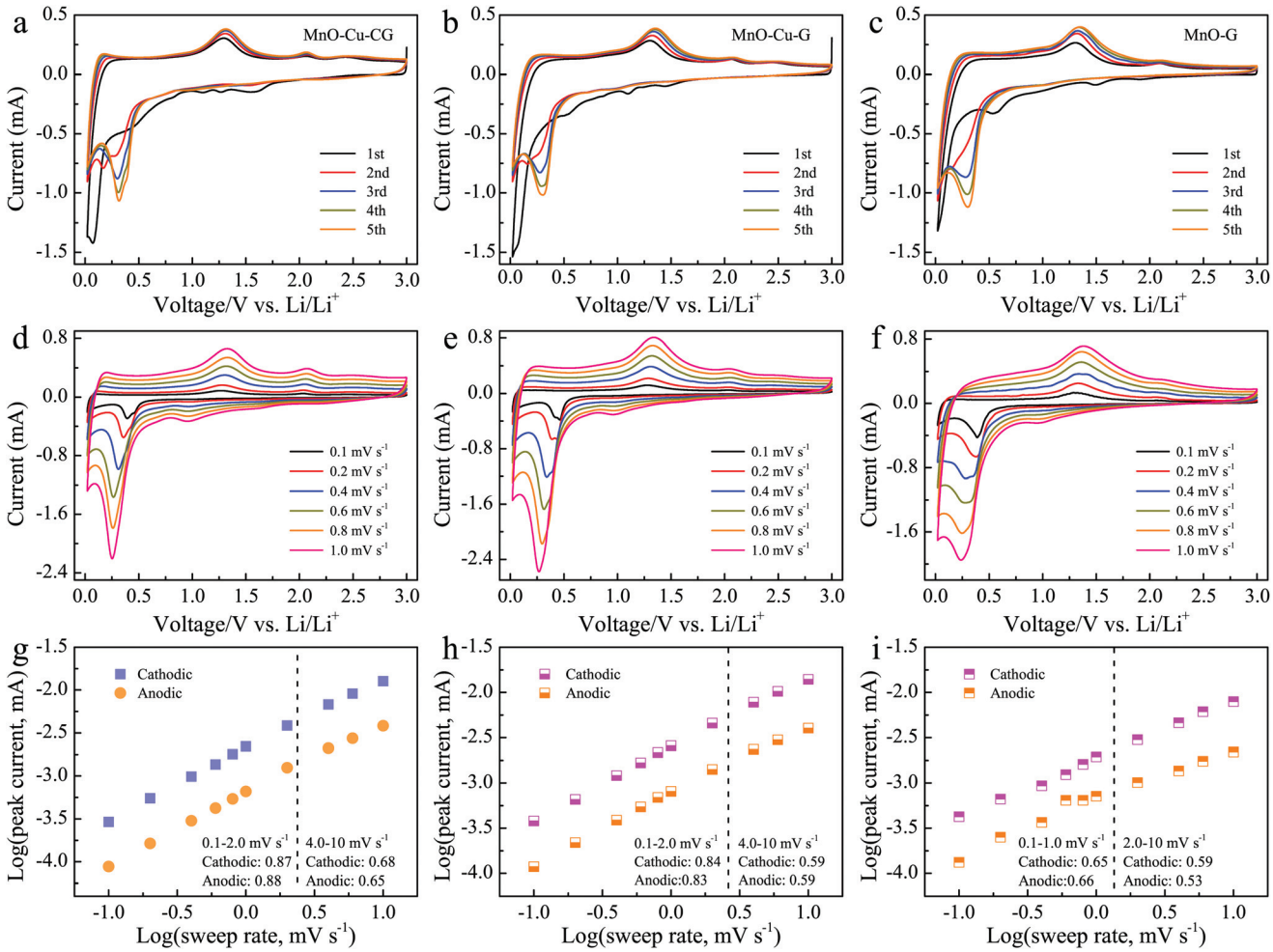

Fig. 3 (a–c) CV curves of the MnO–Cu–CG, MnO–Cu–G, and MnO–G electrodes at a scan rate of 0.5 mV s^{-1} in the range of 0.02–3.0 V *vs.* Li/Li^+; (d–f) CV curves of the MnO–Cu–CG, MnO–Cu–G, and MnO–G electrodes at various sweep rates; and (g–i) determination of the *b* value using the relationship between peak current and scan rate for the MnO–Cu–CG, MnO–Cu–G, and MnO–G electrodes.

peaks with no significant shape change could be clearly observed; however, the peak voltage shifts with the sweep rate for MnO–Cu–CG are quite small in comparison with that of MnO–Cu–G and MnO–G. According to the power-law relationship between the measured current (i) and the scan rate (ν): $i = a\nu^b$, it can be used to analyze the degree of the capacitive effect qualitatively from the slope value (b) of the plots of log(ν)–log(i).[42] In particular, a b value of 0.5 represents a diffusion-controlled lithium storage process whereas a b value of 1 stems from a typical surface-controlled lithium storage process.[42] The log(ν) – log(i) plots for the MnO–Cu–CG electrode are displayed in Fig. 3g. For scan rates ranging from 0.1 to 2.0 mV s^{-1}, the b values of the cathodic and anodic peaks are 0.87 and 0.88, respectively. It confirms that the performance of lithium storage in the MnO–Cu–CG electrode presents capacitive characteristics, conducing to improve the rate capability of active materials. Upon increasing the scan rate to 2.0 mV s^{-1} and above, a decrease in the slope is observed with the b value changing to 0.68 and 0.65 for the cathodic and anodic peaks, respectively, indicating that slow diffusion accounts for the electrochemical kinetics of the electrode. This limitation of kinetics can be attributed to the increase in the ohmic contribution and diffusion constraints at large sweep rates.[33,35] Specifically, the corresponding log(ν)–log(i) plots of the MnO–Cu–G and MnO–G electrodes were determined to investigate the functions of the nanosized Cu and CNT on the pseudocapacitive storage, as shown in Fig. 3h and i. The significantly boosted b values of the MnO–Cu–G electrode compared to the MnO–G electrode demonstrates the fast reaction kinetics of the pseudocapacitive effect, indicating that the incorporation of Cu could promote the charge transfer kinetics in correspondence of the MnO/Cu and MnO/graphene interface.[30] Meanwhile, the higher b values of MnO–Cu–CG than that of MnO–Cu–G, particularly in large sweep rates, indicates enhanced pseudocapacitance contribution in the MnO–Cu–CG electrode. It demonstrates that the presence of CNTs with high electrical conductivity and large surface area can provide a flexible pathway for fast charge transfer, which is beneficial to surface-controlled lithium storage, conducing to improve the rate capability and cycling stability.

The galvanostatic charge/discharge measurements in the range of 0.02–3.0 V are shown in Fig. 4a–c. Obviously, the MnO–Cu–CG electrode delivers an initial discharge and charge capacity of 1113.6 and 772.1 mA h g^{-1}, respectively, with a Coulombic efficiency of 69.3% at 0.1 A h^{-1}. Such initial irreversible capacity loss may be caused by the formation of a SEI layer resulting from electrolyte decomposition and the reaction of the remaining oxygen containing functional groups on CNT/graphene with lithium ions. Despite the initial capacity loss, the well-overlapped charge/discharge profiles after the first cycle demonstrate the excellent reversibility of the MnO–Cu–CG electrode. Interestingly, a discharge capacity of 856.7 mA h g^{-1} is retained after 50 cycles (Fig. 4b). In contrast, the MnO–Cu–G electrode achieves a moderate reversible capacity of 718.8 mA h g^{-1}. Meanwhile, the MnO–G electrode can deliver a high initial discharge and charge capacities of 1239.9 mA h g^{-1} and 736.7 mA h g^{-1}, respectively, in the first cycle; however, the capacity retention fades considerably. The reversible capacity of the MnO–G electrode only remained at 538.7 mA h g^{-1} after 50 cycles. Fig. 4c shows the rate performances of the MnO–Cu–CG, MnO–Cu–G and MnO–G electrodes. The MnO–Cu–CG electrode could deliver a reversible capacity of 749.5, 710.6, 684.4, 627.2, 565.5, 503.1 and 432.4 mA h g^{-1} at 0.05, 0.1, 0.2, 0.4, 0.8, 1.6 and 3.2 A g^{-1}, respectively. When the current density goes back to 0.1 A g^{-1} after 44 cycles, a specific capacity of 783.4 mA h g^{-1} is still recoverable and sustainable up to 861.7 mA h g^{-1} after 70 cycles, highlighting the strong tolerance for the fast charge/discharge process. In comparison, the MnO–Cu–G and MnO–G electrodes exhibit relatively inferior rate performance and poor stability. Such superior performance of MnO–Cu–CG can be mainly attributed to the synergistic effect of CNT/graphene networks and nanosized Cu. The presence of metallic nanocrystals with high electrical conductivity could improve the charge transfer kinetics and prevent the aggregation of active materials. The integration of graphene and porous CNTs provides a large active surface area for pseudocapacitive storage and a flexible pathway for fast charge transfer, as well as the supportive backbone to strengthen the structural integrity. In order to further understand the improved rate capability and cycle stability of the MnO–Cu–CG composite electrode, EIS measurements were conducted for different electrodes. The corresponding Nyquist plots are shown in Fig. 4d. All EIS spectra exhibit a semicircle in the high–medium frequency region and a straight/sloping line in the low frequency region, consistent with the charge transfer process and the semi-infinite Warburg diffusion process, respectively.[43] Obviously, the smallest radius of the semicircle and the steepest line for the MnO–Cu–CG electrode indicate the rapid charge transfer and the lithium ion diffusion kinetics benefitted from the unique structure with multi-dimensional carbon networks and conductive nanosized copper, leading to increased electrochemical performance.

Furthermore, a series of comparative electrochemical measurements were also conducted to investigate the effect of

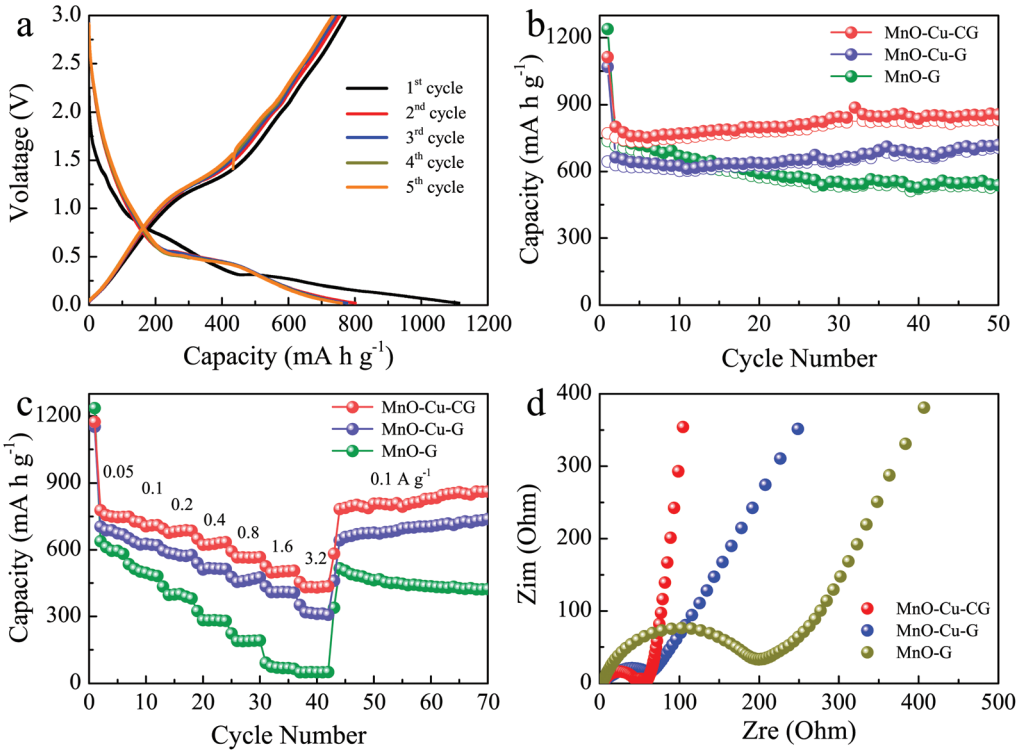

Fig. 4 (a) Galvanostatic charge/discharge curves of the MnO–Cu–CG electrode at 0.1 A g^{-1}; (b) cycling performance of the MnO–Cu–CG, MnO–Cu–G and MnO–G electrodes at 0.1 A g^{-1} for 50 cycles; (c) rate performance of the MnO–Cu–CG, MnO–Cu–G and MnO–G electrodes at various current densities; and (d) Nyquist plots of the MnO–Cu–CG, MnO–Cu–G, and MnO–G electrodes.

Cu and acetylene black content on the lithium storage of the MnO–Cu–CG electrode. MnO–Cu–CG obtained with 0.05, 0.10, and 0.15 g of $Cu(Ac)_2{\cdot}H_2O$ was successively denoted as MnO–0.05Cu–CG, MnO–0.10Cu–CG, and MnO–0.15Cu–CG, respectively. The rate performance of the MnO–Cu–CG samples with different Cu content is shown in Fig. S5.† It can be seen that a typical MnO–Cu–CG (MnO–0.10Cu–CG) delivers an average capacity as high as 756 mA h g^{-1} at 0.1 A g^{-1}, far higher than 590 mA h g^{-1} for MnO–0.05Cu–CG and 614 mA h g^{-1} for MnO–0.15Cu–CG. At a high rate, the capacity of MnO–0.10Cu–CG is a little less than that of MnO–0.15Cu–CG. Despite the lower initial discharge capacity, the more presence of Cu in the composites resulted in more excellent capacity retention, which can be attributed to the highly electronic conductivity of Cu. In general, the MnO–0.10Cu–CG composite shows the best performance combination of high capacity and rate capability at the whole range of current density. In order to better evaluate its natural electrochemical properties, different addition content of acetylene black in the preparation of electrode were made and tested, as shown in Fig. S6.† It can be clearly seen that the rate capability of the MnO–Cu–CG electrode with added 10 wt% acetylene black is still competitive with the MnO–Cu–G electrode with added 20 wt% acetylene black, although there is a decline, further suggesting that MnO–Cu–CG has the intrinsic fast and efficient transfer kinetics for boosting lithium storage.

To further demonstrate that the ability of the MnO–Cu–CG electrode is practically applicable for LIBs, a long-term cycling test of a typical MnO–Cu–CG was conducted at a current density of 0.8 A g^{-1} and the result is shown in Fig. 5a. Interestingly, the cycling process of the MnO–Cu–CG electrode seems to include four different stages based on the variation

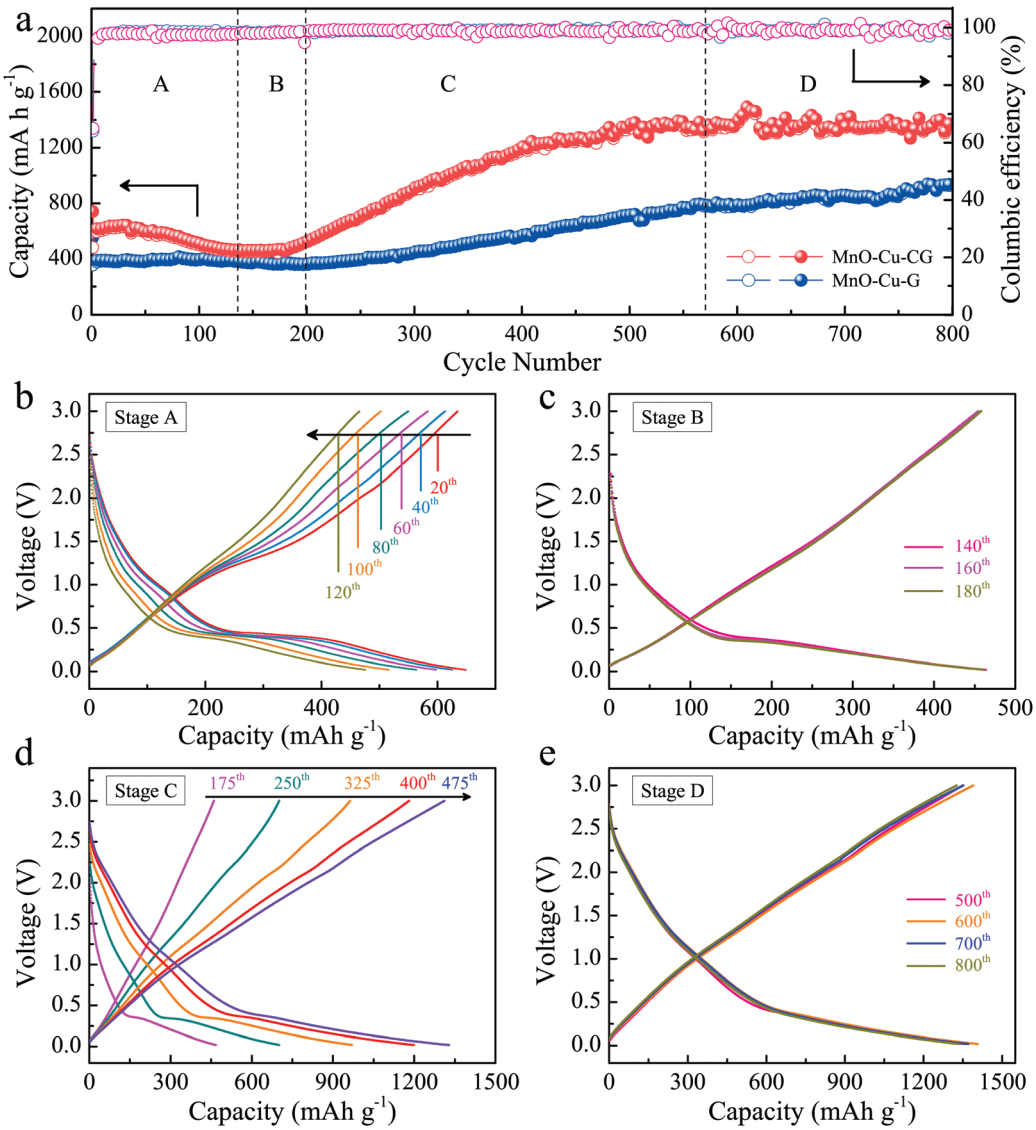

Fig. 5 (a) Cycling performance comparison between the MnO–Cu–CG and MnO–Cu–G electrodes at 0.8 A g^{-1}. Galvanostatic charge/discharge curves of the MnO–Cu–CG electrode for (b) stage A, (c) stage B, (d) stage C, and (e) stage D.

of the specific capacity as illustrated in Fig. 5b–e. Stage A: From the first cycle to the 130th cycle, a clear drop in specific capacity is recorded (Fig. 5b). The discharge capacity at the first cycle is 741 mA h g^{-1}, which goes through a fading down to 465 mA h g^{-1} after 130 cycles. Stage B: In the range of 130–175 cycles, the specific capacity stabilizes, and the voltage profiles of the 140th, 160th and 180th cycles overlap completely in the whole voltage range (Fig. 5c), exhibiting close-to-99% Coulombic efficiency. Stage C: Till the 500th cycle, the electrode is activated and exhibits an ever-increasing lithium storage capacity. The charge–discharge profiles of the 175th, 225th, 325th, 400th and 475th cycles are shown in Fig. 5d, which clearly shows the capacity rise behavior. Stage D: Beyond the 500th cycle, a nearly constant capacity with close-to-100% Coulombic efficiency can be observed. The galvanostatic charge/discharge curves of the 500th, 600th, 700th and 800th cycles overlapped completely in the whole voltage range (Fig. 5e), demonstrating the purely reversible electrochemical reaction and the superior cycling stability of the MnO–Cu–CG electrode. Such a capacity fading–reactivation phenomenon is commonly observed in nanostructured metal oxide electrodes.[44,45] The capacity loss is induced by the fluctuation of the SEI film and the decomposition of the electrolyte. The consequent increase in capacity is due to the gradual activation of MnO induced by the gradually opened lithium ion transport channel,[46] the formation of an electrochemically active gel-like film,[36] the transformation of MnO into small size nanograins upon cycling,[27] and the generation of higher oxidation state manganese by Li_2O oxidation.[21] Moreover, the high surface area and porosity of MnO–Cu–CG contribute significantly to the capacitive-like lithium storage with further cycling, resulting in a steadily strengthened pseudocapacitance even greater than the theoretical capacity value of MnO.[45] In the same case, the MnO–Cu–G electrode can only possess a lower capacity of 938.3 mA h g^{-1} after 800 cycles but goes through more cycles to achieve stability. Moreover, the cyclic capacity and stability of the MnO–Cu–CG electrode at 3.2 A g^{-1} over 2000 cycles are also superior to those of the MnO–Cu–G electrode (Fig. S7†), further confirming that the addition of CNTs with special properties is useful to improve the electrical conductivity and surface pseudocapacitive storage.

Encouraged by the intriguing electrochemical performance presented above, rate testing at an even higher current density of 8 A g^{-1} was conducted. As shown in Fig. 6a, the MnO–Cu–CG electrode still delivers high average reversible capacities of 776, 690, 626, 564 and 471 mA h g^{-1} when cycled at current densities of 0.1, 0.5, 1, 2 and 5 A g^{-1}, respectively. Impressively, an average discharge capacity of 409.5 mA h g^{-1} can be achieved even at an ultrahigh current rate of 8 A g^{-1}, which is demonstrated in the charge and discharge curves in Fig. S8.† Moreover, the reversible capacity could swiftly return to 804 mA h g^{-1} when the current was switched from 8 to 0.1 A g^{-1}, indicating a superior restorability. Such boosted electrochemical properties can be attributed to the unique intrinsic structure characteristics of uniform anchored multiscaled MnO–Cu grains in the surface of 3D conductive networks. In addition to the ultrahigh rate capability, the unique architecture also endows MnO–Cu–CG with remarkable cycling stability at ultrahigh current density, as demonstrated in Fig. 6b. Tested at 5 A g^{-1}, the capacity undergoes a fading down in the

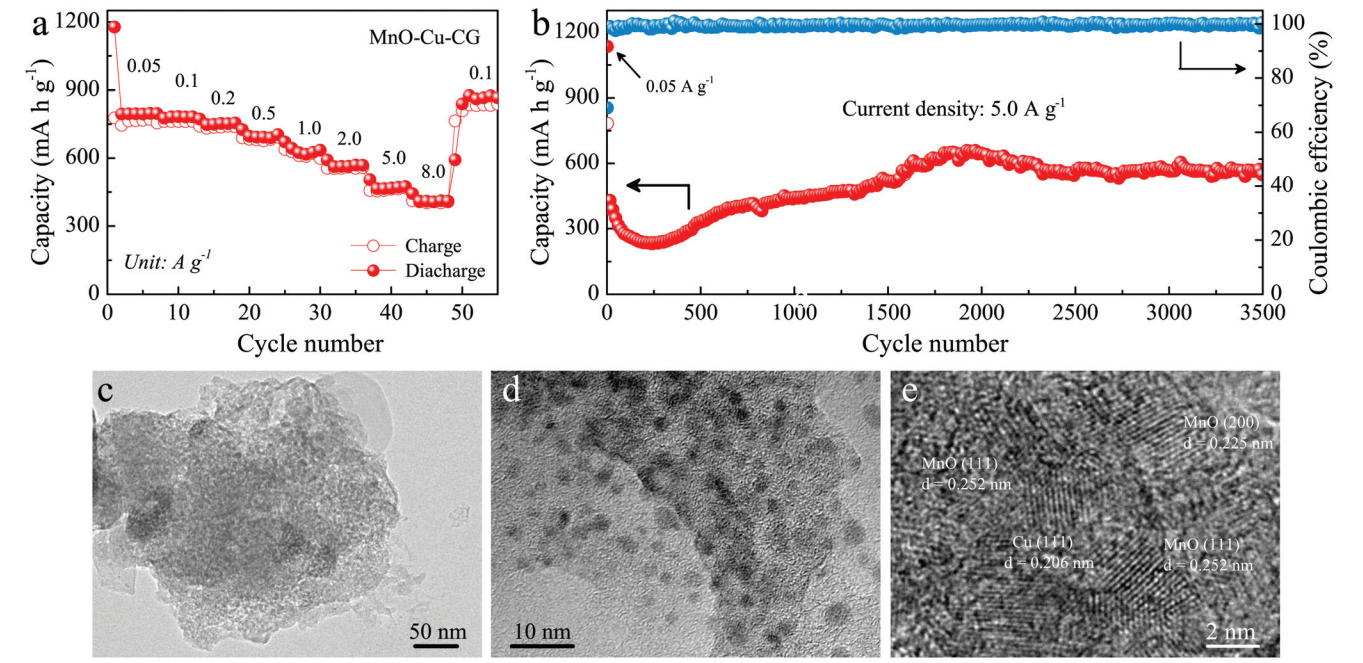

Fig. 6 (a) Rate performance of the MnO–Cu–CG electrode at various current densities; (b) cycling performance and Coulombic efficiency of the MnO–Cu–CG electrode cycled at 5 A g^{-1} for 3500 cycles, at 0.05 A g^{-1} for the first three cycles; and (c) TEM, (d) high-magnification TEM, and (e) HRTEM images of the MnO–Cu–CG electrode after 3500 cycles at 5 A g^{-1}.

initial 200 cycles, following the increase in capacity to 662.2 mA h g^{-1}. With prolonged cycling over 3500 cycles, the MnO–Cu–CG electrode can still deliver a stable reversible capacity as high as 557.9 mA h g^{-1} with nearly 100% Coulombic efficiency. The comparison of the lithium storage property of the MnO–Cu–CG electrode and that of the previously reported MnO-based anode materials has been summarized in Table 1.

To investigate the relationship between microstructure features and cycling stability, the TEM analysis of the MnO–Cu–CG electrode after 3500 cycles at 5 A g^{-1} was carried out. As shown in Fig. 6c, the closely packed MnO–Cu grains are anchored to the CNT/graphene networks after extended cycling processes. The nanostructures among the MnO–Cu hybrids and the supported conductive CNT/graphene could act as fast channels for ion and electron transport in the MnO crystals, promoting the reaction kinetics of the conversion reactions. The magnified TEM image in Fig. 6d shows that the nanosized MnO–Cu nanoparticles (dark zones) are well dispersed on the conductive matrix (bright zones) and there is no clear cluster aggregation in the electrode. The nanosized Cu effectively suppresses the Mn coarsening in the lithiated MnO during cycling, which maintained fast interdiffusion kinetics between the nanoscale Mn/Li_2O interfaces. Moreover, the conductive networks accommodate well the large volume change of MnO and provide large reaction sites on the surface area, resulting in boosted pseudocapacitive storage. As shown in Fig. 6e, the HRTEM image further reveals that the cycled electrode is largely in an amorphous state except for some embedded Cu and MnO nanocrystals with small dimensions of around 2–3 nm, enabling spatially confined high and fast charge storage for capacity reactivation due to the downsizing effect.[39,46]

Table 1 The cycling performance comparison of the MnO–Cu–CG electrode and previously reported MnO-based anode materials

MnO-based materials	Rate [A g^{-1}]	Capacity [mA h g^{-1}]	Cycles [times]	Ref.
MnO/C spheres	0.2	1040	500	20
3D MnO/C–N	0.3	513	400	41
MnO@C/RGO	0.38	863	160	24
MnO-PCNTs	0.5	573	300	25
MnO/C spheres	0.8	800	100	22
MnO/graphene	2.0	843	400	36
MnO/C peapods	2.0	525	1000	26
MnO/N-GSC/GR	2.0	812	1000	27
MnO@N–C/rGO	2.0	425	1300	40
3D MnO/N–C	4.0	310	3000	19
MnO/C hybrid	5.0	1467	2000	38
RGO–MnO–RGO	15.0	379	4000	37
MnO@C peapods	0.3	932	400	47
MnO/G nanowires	0.5	930	470	48
MnO@C/CNTs	0.5	1266	500	49
MnO/C microrods	0.6	936	100	50
MnO@NC spheres	1.0	690	150	51
MnO/C nanorods	1.0	1211	700	52
MnO/C nanofibers	1.0	575	200	53
MnO/C nanowires	1.0	480	600	54
MnO@C/N–C	1.0	1268	700	55
G/MnO@C/G	4.0	471	4000	56
MnO–Cu–CG	**0.8**	**1334.2**	**800**	**This work**
	5.0	**557.9**	**3500**	

The above results evidently suggest that the 3D MnO–Cu–CG electrode exhibits high capacity, impressive long life and rate performance, which can be ascribed to the synergistic effects of nanosized Cu and unique interconnected conductive networks. The highly conductive Cu and CNT/graphene could facilitate the fast charge transport for electrochemical reactions over shorter distances and minimise excessive stress developing in the electrode during cycling. In addition, the MnO particles in the MnO–Cu–CG composite can be refined to nanosize after cycling, resulting in relatively small volumetric strain and stress upon cycling. Moreover, the interpenetrated CNT/graphene networks provide enlarged accessible surface area and multidimensional pathways. It is more suitable for the full contact between the electrode and the electrolyte and the transportation of lithium ions into the internal parts of the electrode. In particular, the nanosized Cu and conductive framework could synergistically improve the transfer kinetics for high active surface/interface and prevent the aggregation of MnO, ensuring long-life stability and excellent rate performance.

4. Conclusions

In conclusion, a quaternary hybrid MnO–Cu–CNT/graphene has been constructed to pursue high rate capability and long lifetimes in MnO-based anodes for LIBs. It has been demonstrated that the well-distributed ultrafine MnO–Cu grains on 3D conductive networks successfully inhibit MnO coarsening to achieve fast charge transfer and sufficient sites for electrochemical reaction in high active surface/interface, resulting in highly reversible conversion reactions and boosted pseudocapacitive storage. The simply prepared MnO–Cu–CG electrode delivers an ultrahigh capacity (1334.2 mA h g^{-1}) and an excellent rate capability (409.5 mA h g^{-1} at 8 A g^{-1}) as well as a superior cycling performance (557.9 mA h g^{-1} over 3500 cycles at 5 A g^{-1}). It is hoped that the excellent electrochemical performance of the simple fabricated MnO–Cu–CNT/graphene composite opens up a new avenue toward the development of similar conversion-type anode materials for large capacity and long lifespan lithium storage.

Conflicts of interest

There are no conflicts to declare.

Acknowledgements

This work was financially supported by the Major State Basic Research Development Program of China (Grant No. 2013CB922300), the Natural and Science Foundation of China (Grant No. 61674057, 11374097, 61376129, 61504156, and 61227902), the Projects of Science and Technology

Commission of Shanghai Municipality (Grant No. 15JC1401600), and the Program for Professor of Special Appointment (Eastern Scholar) at Shanghai Institutions of Higher Learning.

References

1 M. Armand and J. M. Tarascon, *Nature*, 2008, **451**, 652–657.
2 J. B. Goodenough, *Energy Environ. Sci.*, 2014, **7**, 14–19.
3 Y. X. Tang, Y. Y. Zhang, W. L. Li, B. Ma and X. D. Chen, *Chem. Soc. Rev.*, 2015, **44**, 5926–5940.
4 N. Wang, Z. C. Bai, Y. T. Qian and J. Yang, *Adv. Mater.*, 2016, **28**, 4126–4133.
5 Y. Ma, R. Younesi, R. J. Pan, C. J. Liu, J. F. Zhu, B. Q. Wei and K. Edstrŏm, *Adv. Funct. Mater.*, 2016, **26**, 6797–6806.
6 L. Q. Zong, Y. Jin, C. Liu, B. Zhu, X. Z. Hu, Z. D. Lu and J. Zhu, *Nano Lett.*, 2016, **16**, 7210–7215.
7 D. H. Youn, A. Heller and C. B. Mullins, *Chem. Mater.*, 2016, **28**, 1343–1347.
8 J. Hwang, S. H. Woo, J. Shim, C. Jo, K. T. Lee and J. Lee, *ACS Nano*, 2013, **7**, 1036–1044.
9 J. Jiang, Y. Li, J. Liu, X. Huang, C. Yuan and X. W. Lou, *Adv. Mater.*, 2012, **24**, 5166–5180.
10 M. V. Reddy, G. V. S. Rao and B. V. R. Chowdari, *Chem. Rev.*, 2013, **113**, 5364–5457.
11 M. Srivastava, J. Singh, T. Kuila, R. K. Layek, N. H. Kime and J. H. Lee, *Nanoscale*, 2015, **7**, 4820–4868.
12 R. Z. Hu, G. H. Waller, Y. K. Wang, Y. Chen, C. Y. Yang, W. J. Zhou, M. Zhu and M. L. Liu, *Nano Energy*, 2015, **18**, 232–244.
13 Y. Zhao, T. T. Liu, H. Xia, L. Zhang, J. X. Jiang, M. Shen, J. F. Ni and L. J. Gao, *J. Mater. Chem. A*, 2014, **2**, 13854–13858.
14 L. F. Jiang, B. H. Lin, X. M. Li, X. F. Song, H. Xia, L. Li and H. B. Zeng, *ACS Appl. Mater. Interfaces*, 2016, **8**, 2680–2687.
15 Z. N. Deng, H. Jiang, Y. J. Hu, Y. Liu, L. Zhang, H. L. Liu and C. Z. Li, *Adv. Mater.*, 2017, **29**, 1603020.
16 H. Su, Y. F. Xu, S. C. Feng, Z. G. Wu, X. P. Sun, C. H. Shen, J. Q. Wang, J. T. Li, L. Huang and S. G. Sun, *ACS Appl. Mater. Interfaces*, 2015, **7**, 8488–8494.
17 J. Tang, W. Liu, H. L. Wang and A. Gomez, *Adv. Mater.*, 2016, **28**, 10298–10303.
18 J. G. Wang, D. D. Jin, H. Y. Liu, C. B. Zhang, R. Zhou, C. Shen, K. Y. Xie and B. Q. Wei, *Nano Energy*, 2016, **22**, 524–532.
19 W. Zhang, J. Z. Sheng, J. Zhang, T. He, L. Hu, R. Wang, L. Q. Mai and S. C. Mu, *J. Mater. Chem. A*, 2016, **4**, 16936–16945.
20 S. B. Wang, C. L. Xiao, Y. L. Xing, H. Z. Xu and S. C. Zhang, *J. Mater. Chem. A*, 2015, **3**, 15591–15997.
21 J. C. Guo, Q. Liu, C. S. Wang and M. R. Zachariah, *Adv. Funct. Mater.*, 2012, **22**, 803–811.
22 Y. Xia, Z. Xiao, X. Dou, H. Huang, X. H. Lu, R. J. Yan, Y. P. Gan, W. J. Zhu, J. P. Tu, W. K. Zhang and X. Y. Tao, *ACS Nano*, 2013, **7**, 7083–7092.
23 S. B. Wang, Y. B. Ren, G. R. Liu, Y. L. Xing and S. C. Zhang, *Nanoscale*, 2014, **6**, 3508–3512.
24 D. H. Liu, H. Y. Lu, X. L. Wu, B. H. Hou, F. Wan, S. D. Bao, Q. Y. Yan, H. M. Xie and R. S. Wang, *J. Mater. Chem. A*, 2015, **3**, 19738–19746.
25 Q. T. Zhang, Q. Q. Dai, M. Li, X. M. Wang and A. Li, *J. Mater. Chem. A*, 2016, **4**, 19132–19139.
26 H. Jiang, Y. J. Hu, S. J. Guo, C. Y. Yan, P. S. Lee and C. Z. Li, *ACS Nano*, 2014, **8**, 6038–6046.
27 Y. Zhang, P. H. Chen, X. Gao, B. Wang, H. Liu, H. Wu, H. K. Liu and S. X. Dou, *Adv. Funct. Mater.*, 2016, **26**, 7754–7765.
28 H. T. Tan, X. H. Rui, Z. Y. Lu, C. Xu, W. L. Liu, H. H. Hng and Q. Y. Yan, *J. Phys. Chem. C*, 2014, **118**, 17452–17460.
29 L. Fan, Y. C. Zhu, J. J. Zhang, J. W. Liang, L. L. Wang, D. H. Wei, X. N. Li and Y. T. Qian, *Electrochim. Acta*, 2014, **121**, 21–26.
30 R. Z. Hu, Y. P. Ouyang, T. Liang, X. Tang, B. Yuan, J. Liu, L. Zhang, L. C. Yang and M. Zhu, *Energy Environ. Sci.*, 2017, **10**, 2017–2029.
31 T. Brezesinski, J. Wang, S. H. Tolbert and B. Dunn, *Nat. Mater.*, 2010, **9**, 146–151.
32 D. L. Chao, C. R. Zhu, P. H. Yang, X. H. Xia, J. L. Liu, J. Wang, X. F. Fan, S. V. Savilov, J. Y. Lin, H. J. Fan and Z. X. Shen, *Nat. Commun.*, 2016, **7**, 12122.
33 V. Augustyn, J. Come, M. A. Lowe, J. W. Kim, P. L. Taberna, S. H. Tolbert, H. D. Abruña, P. Simon and B. Dunn, *Nat. Mater.*, 2013, **12**, 518–522.
34 M. Sathiya, A. S. Prakash, K. Ramesha, J. M. Tarascon and A. K. Shukla, *J. Am. Chem. Soc.*, 2011, **133**, 16291–16299.
35 C. J. Chen, Y. W. Wen, X. L. Hu, X. L. Ji, M. Y. Yan, L. Q. Mai, P. Hu, B. Shan and Y. H. Huang, *Nat. Commun.*, 2015, **6**, 6929.
36 Y. M. Sun, X. L. Hu, W. Luo, F. F. Xia and Y. H. Huang, *Adv. Funct. Mater.*, 2013, **23**, 2436–2444.
37 T. Z. Yuan, Y. Z. Jiang, W. P. Sun, B. Xiang, Y. Li, M. Yan, B. Xu and S. X. Dou, *Adv. Funct. Mater.*, 2016, **26**, 2198–2206.
38 Y. Xiao and M. H. Cao, *ACS Appl. Mater. Interfaces*, 2015, **7**, 12840–12849.
39 L. Chen, H. Jiang, H. Jiang, H. X. Zhang, S. J. Guo, Y. J. Hu and C. Z. Li, *Adv. Energy Mater.*, 2017, **7**, 1602782.
40 W. Zhang, J. N. Li, J. Zhang, J. Z. Sheng, T. He, M. Y. Tian, Y. F. Zhao, C. J. Xie, L. Q. Mai and S. C. Mu, *ACS Appl. Mater. Interfaces*, 2017, **9**, 12680–12686.
41 L. F. Chen, S. X. Ma, S. Lu, Y. Feng, J. Zhang, S. Xin and S. H. Yu, *Nano Res.*, 2017, **10**, 1–11.
42 H. Y. Wang, H. Jiang, Y. J. Hua, P. Saha, Q. L. Cheng and C. Z. Li, *Chem. Eng. Sci.*, 2017, **174**, 104–111.
43 J. L. Liu, Z. Chen, S. Chen, B. Zhang, J. Wang, H. H. Wangle, B. B. Tian, M. H. Chen, X. F. Fan, Y. Z. Huang, T. C. Sum, J. Y. Lin and Z. X. Shen, *ACS Nano*, 2017, **11**, 6911–6920.
44 Y. Z. Jiang, D. Zhang, Y. Li, T. Z. Yuan, N. Bahlawane, C. Liang, W. P. Sun, Y. H. Lu and M. Yan, *Nano Energy*, 2014, **4**, 23–30.

45 S. Zhu, J. J. Li, X. Y. Deng, C. N. He, E. Z. Liu, F. He, C. S. Shi and N. Q. Zhao, *Adv. Funct. Mater.*, 2017, **27**, 1605017.
46 R. Liu, S. Q. Zhao, M. M. Zhang, F. Feng and Q. Shen, *Chem. Commun.*, 2015, **51**, 5728–5731.
47 S. B. Wang, Y. L. Xing, C. L. Xiao, H. Z. Xu and S. C. Zhang, *J. Power Sources*, 2016, **307**, 11–16.
48 S. Zhang, L. X. Zhu, H. H. Song, X. H. Chen and J. S. Zhou, *Nano Energy*, 2014, **10**, 172–180.
49 X. J. Jiang, W. Yu, H. Wang, H. Y. Xu, X. Z. Liu and Y. Ding, *J. Mater. Chem. A*, 2016, **4**, 920–925.
50 D. Sun, Y. G. Tang, D. L. Ye, J. Yan, H. S. Zhou and H. Y. Wang, *ACS Appl. Mater. Interfaces*, 2017, **9**, 5254–5262.
51 L. L. Zhang, D. H. Ge, G. L. Qu, J. W. Zheng, X. Q. Cao and H. W. Gu, *Nanoscale*, 2017, **9**, 5451–5457.
52 X. M. Tang, G. Sui, Q. Cai, W. H. Zhong and X. P. Yang, *J. Mater. Chem. A*, 2016, **4**, 2082–2088.
53 B. Liu, X. L. Hu, H. H. Xu, W. Luo, Y. M. Sun and Y. H. Huang, *Sci. Rep.*, 2014, **4**, 4229.
54 J. G. Wang, C. B. Zhang, D. D. Jin, K. Y. Xie and B. Q. Wei, *J. Mater. Chem. A*, 2015, **3**, 13699–13705.
55 W. M. Chen, L. Qie, Y. Shen, Y. M. Sun, L. X. Yuan, X. L. Hu, W. X. Zhang and Y. H. Huang, *Nano Energy*, 2013, **2**, 412–418.
56 J. Zhang, W. Zhang, T. He, I. S. Amiinu, Z. K. Kou, J. N. Li and S. C. Mu, *Carbon*, 2017, **115**, 95–104.